Electronic Supplementary Information (ESI)

Nitrides: A Promising Class of Nonlinear Optical Material Candidates

Xin Zhao [a, c], Chensheng Lin [a], Haotian Tian [a, c], Chao Wang [a, c], Ning Ye [d] and Min Luo *[a, b]

[a] *Key Laboratory of Optoelectronic Materials Chemistry and Physics, Fujian Institute of Research on the Structure of Matter, Chinese Academy of Sciences, Fuzhou, Fujian 350002, China*

E-mail: lm8901@fjirsm.ac.cn

[b] *Fujian Science & Technology Innovation Laboratory for Optoelectronic Information of China, Fuzhou, Fujian 350108, China*

[c] *University of Chinese Academy of Sciences, Beijing 100049, China*

[d] *Tianjin Key Laboratory of Functional Crystal Materials, Institute of Functional Crystal, Tianjin University of Technology, Tianjin 300384, China*

Table of Contents

Theoretical calculations

Figures

Figure S1 Crystal structure of $LiSi_2N_3$ (a); coordination of Ba^{2+} / Pb^{2+} in $Ba_2Si_5N_8$ / $Pb_2Si_5N_8$ (b).

Figure S2 Calculated band structure (HSE06) of GaN (a), AlN (b), $LiSi_2N_3$ (c), $LiGe_2N_3$ (d), $MgSiN_2$ (e) and $MgGeN_2$ (f).

Figure S3 Calculated band structure (HSE06) of $BeSiN_2$ (a), $ZnSiN_2$ (b), $ZnGeN_2$ (c), Zn_3MoN_4 (d), Mg_2PN_3 (e) and Zn_2PN_3 (f).

Figure S4 Calculated band structure (HSE06) of $MgSbN_3$ (a), $LiPN_2$ (b), $CuPN_2$ (c), LiSiON (d), Li_2PO_2N (e) and $NaPN_2$ (f).

Figure S5 Calculated band structure (HSE06) of $NaSi_2N_3$ (a), $NaGe_2N_3$ (b), $CaGeN_2$ (c), CaP_2N_4 (d), SrP_2N_4 (e) and $Sr_2Si_5N_8$ (f).

Figure S6 Calculated band structure (HSE06) of $Ba_2Si_5N_8$ (a), $SrSi_7N_{10}$ (b), $BaSi_7N_{10}$ (c), $SrSi_6N_8$ (d), α-$Ca_2Si_5N_8$ (e) and β-$Ca_2Si_5N_8$ (f).

Figure S7. Calculated band structure (HSE06) of $Ca_3Al_2N_4$ (a), $SrAlSi_4N_7$ (b), $SrYSi_4N_7$ (c), $LaSi_3N_5$ (d), $Pb_2Si_5N_8$ (e) and NaSnN (f).

Figure S8 Calculated band structure (HSE06) of Na_3MoN_4 (a), Na_3WN_4 (b), $Ba_3B_2N_4$ (c), $Ba_5Si_2N_6$ (d).

Figure S9 Total density/partial density of states (PDOS) of GaN (a), AlN (b), $LiSi_2N_3$ (c), $LiGe_2N_3$ (d), $MgSiN_2$ (e), and $MgGeN_2$ (f).

Figure S10 Total density/partial density of states (PDOS) of $BeSiN_2$ (a), $ZnSiN_2$ (b), $ZnGeN_2$ (c), Zn_3MoN_4 (d), Mg_2PN_3 (e), and Zn_2PN_3 (f).

Figure S11 Total density/partial density of states (PDOS) of $MgSbN_3$ (a), $LiPN_2$ (b), $CuPN_2$ (c), LiSiON (d), Li_2PO_2N (e), and $NaPN_2$ (f).

Figure S12 Total density/partial density of states (PDOS) of $NaSi_2N_3$ (a), $NaGe_2N_3$ (b), $CaGeN_2$ (c), CaP_2N_4 (d), SrP_2N_4 (e), and $Sr_2Si_5N_8$ (f).

Figure S13 Total density/partial density of states (PDOS) of $Ba_2Si_5N_8$ (a), $SrSi_7N_{10}$ (b), $BaSi_7N_{10}$ (c), $SrSi_6N_8$ (d), α-$Ca_2Si_5N_8$ (e), and β-$Ca_2Si_5N_8$ (f).

Figure S14 Total density/partial density of states (PDOS) of $Ca_3Al_2N_4$ (a), $SrAlSi_4N_7$ (b), $SrYSi_4N_7$ (c), $LaSi_3N_5$ (d), $Pb_2Si_5N_8$ (e), and Na_3MoN_4 (f).

Figure S15 Total density/partial density of states (PDOS) of Na_3WN_4 (a), $Ba_3B_2N_4$ (c), and $Ba_5Si_2N_6$ (c).

Figure S16 Calculated frequency-dependent coefficients of GaN (a), AlN (b), $LiSi_2N_3$ (c), $LiGe_2N_3$ (d), $MgSiN_2$ (e), and $MgGeN_2$ (f).

Figure S17 Calculated frequency-dependent coefficients of $BeSiN_2$ (a), $ZnSiN_2$ (b), $ZnGeN_2$ (c), Zn_3MoN_4 (d), Mg_2PN_3 (e), and Zn_2PN_3 (f).

Figure S18 Calculated frequency-dependent coefficients of $MgSbN_3$ (a), $LiPN_2$ (b), $CuPN_2$ (c), Zn_2NCl (d), Zn_2NBr (e), and LiSiON (f).

Figure S19 Calculated frequency-dependent coefficients of $LiPO_2N$ (a), $NaPN_2$ (b), $NaSi_2N_3$ (c), $NaGe_2N_3$ (d), $CaGeN_2$ (e), and CaP_2N_4 (f).

Figure S20 Calculated frequency-dependent coefficients of SrP_2N_4 (a), $Sr_2Si_5N_8$ (b), $Ba_2Si_5N_8$ (c), $SrSi_7N_{10}$ (d), $BaSi_7N_{10}$ (e), and $SrSi_6N_8$ (f)

Figure S21 Calculated frequency-dependent coefficients of α-$Ca_2Si_5N_8$ (a), β-$Ca_2Si_5N_8$ (b), $Ca_3Al_2N_4$ (c), $SrAlSi_4N_7$ (d), $SrYSi_4N_7$ (e), and $LaSi_3N_5$ (f).

Figure S22 Calculated frequency-dependent coefficients of $Pb_2Si_5N_8$ (a), Na_3MoN_4 (b), Na_3WN_4 (c), $Ba_3B_2N_4$ (d), and $Ba_5Si_2N_6$ (e).

Figure S23 The calculated refractive index dispersion curves and birefringence of GaN (a), AlN (b), $LiSi_2N_3$ (c), $LiGe_2N_3$ (d), $MgSiN_2$ (e), and $MgGeN_2$ (f).

Figure S24 The calculated refractive index dispersion curves and birefringence of $BeSiN_2$ (a), $ZnSiN_2$ (b), $ZnGeN_2$ (c), Zn_3MoN_4 (d), Mg_2PN_3 (e), and Zn_2PN_3 (f).

Figure S25 The calculated refractive index dispersion curves and birefringence of $MgSbN_3$ (a), $LiPN_2$ (b), $CuPN_2$ (c), Zn_2NCl (d), Zn_2NBr (e), and LiSiON (f).

Figure S26 The calculated refractive index dispersion curves and birefringence of $LiPO_2N$ (a), $NaPN_2$ (b), $NaSi_2N_3$ (c), $NaGe_2N_3$ (d), $CaGeN_2$ (e), and CaP_2N_4 (f).

Figure S27 The calculated refractive index dispersion curves and birefringence of SrP_2N_4 (a), $Sr_2Si_5N_8$ (b), $Ba_2Si_5N_8$ (c), $SrSi_7N_{10}$ (d), $BaSi_7N_{10}$ (e), and $SrSi_6N_8$ (f).

Figure S28 The calculated refractive index dispersion curves and birefringence of α-$Ca_2Si_5N_8$ (a), β-$Ca_2Si_5N_8$ (b), $Ca_3Al_2N_4$ (c), $SrAlSi_4N_7$ (d), $SrYSi_4N_7$ (e), and $LaSi_3N_5$ (f).

Figure S29 The calculated refractive index dispersion curves and birefringence of $Pb_2Si_5N_8$ (a), Na_3MoN_4 (b), Na_3WN_4 (c), $Ba_3B_2N_4$ (d), and $Ba_5Si_2N_6$ (e).

References

Theoretical calculations

The electronic band structure, linear optical properties, and nonlinear optical (NLO) properties of potential NLO nitrides were calculated by the plane wave pseudo-potential method in Materials Studio using CASTEP package [1]. The exchange and correlative potential of electron-electron interactions were represented by generalized gradient approximation (GGA) in the scheme of Perdew-Burke-Ernzerhof (PBE) [2]. Furthermore, the interaction of the electrons with ion cores was represented by the norm-conserving pseudopotentials [3, 4], and the valence electrons were expressed as: Li $2s^1$, Na $2s^22p^63s^1$, Be $2s^2$, Mg $2s^22p^63s^2$, Ca $3s^23p^64s^2$, Sr $4s^24p^65s^2$, Ba $5s^25p^66s^2$, Zn $3d^{10}4s^2$, Cu $3d^{10}4s^1$, B $2s^22p^1$, Al $3s^23p^1$, Ga $3d^{10}4s^24p^1$, Si $3s^23p^2$, Ge $4s^24p^2$, Sn $5s^25p^2$, Pb $4f^{14}5d^{10}6s^26p^2$, P $3s^23p^3$, Sb $4d^{10}5s^25p^3$, Y $4d^{15}s^2$, La $5d^{16}s^2$, Mo $4d^55s^1$, W $4f^{14}5d^46s^2$, Cl $3s^23p^5$, Br $4s^24p^5$, and N $2s^22p^3$, a plane-wave cut-off energy more than the element minimum value was set throughout the calculations. The dense k-points sampling of less than 0.05 $Å^{-1}$ for the target compounds were adopted for the good convergence of electronic structures and optical properties. Moreover, the other calculated parameters utilization and convergent criteria were in line with the default values of the CASTEP code.

The experimental band gaps of some nitrides are unknown. In order to accurately estimate their band gaps and subsequently carry out calculations for NLO properties, the hybrid functional Heyd-Scuseria-Ernzerhof (HSE06) methodology was adopted because this hybrid functional can precisely predict band gaps comparable to experimental values [5-7].

The second-order NLO coefficients were calculated using the susceptibility formula based on the perturbation method of Sipe [8, 9], and the susceptibility formula obtained by defining the δ function.

For the electronic transition from valence to conduction bands (V-C process):

$$\chi_{abc}^{(2,I)}(-2\omega;\omega,\omega) = \frac{-e^3h^3}{m^3\Omega}\sum_{ijlK}^{i\in V,j\in C,i\neq l}\frac{3\eta}{\left|0.5E_{ji}(K)-E_{li}(K)\right|}\left[\frac{\delta\left(E-0.5E_{ji}(K)\right)}{0.25E_{ji}^4(K)}+\frac{\delta\left(E-E_{li}(K)\right)}{4E_{li}^4(K)}\right]P_{abc}(P_{ij}^a$$

(S1)

For V-V and V-C mixing processes:

$$\chi_{abc}^{(2,II)}(-2\omega;\omega,\omega) = \frac{-e^3h^3}{m^3\Omega}\sum_{ijlK}^{il\in V,j\in C,i\neq l}\frac{3\eta}{|0.5E_{ji}(K)-E_{jl}(K)|}\left[\frac{\delta(E-0.5E_{ji}(K))}{0.25E_{ji}^4(K)}+\frac{\delta(E-E_{jl}(K))}{4E_{jl}^4(K)}\right]P_{abc}(P_l^{\prime}$$

(S2)

Where,

$$P_{abc}\left(P_{li}^a(K)P_{ij}^b(K)P_{jl}^c(K)\right) = 0.5P_{bc}(p_{li}^a(K)p_{ij}^b(K)p_{jl}^c(K)+p_{ij}^a(K)p_{jl}^b(K)p_{lj}^c(K)+p_{jl}^a(K)p_{li}^b(K)p_{ij}^c(K))$$

The δ(x) is a δ function and η is damping factor in the formulas (S1) and (S2). The moment matrix elements $p_{ij}(K)$ and the energy $E_{ij}(K)$ were derived from the density functional theory (DFT) calculation integrating with CASTEP code, and the imaginary part of $\chi_{abc}^{(2)} = \chi_{abc}^{(2,I)} + \chi_{abc}^{(2,II)}$ can obtained by using formulas (S1) and (S2). The real part $\chi^{(2)}$ obtained by Kramers-Kronig transform from the imaginary part. Here note that $\chi^{(2)} = [(r\chi^{(2)})^2 + (i\chi^{(2)})^2]^{1/2}$.

Figures

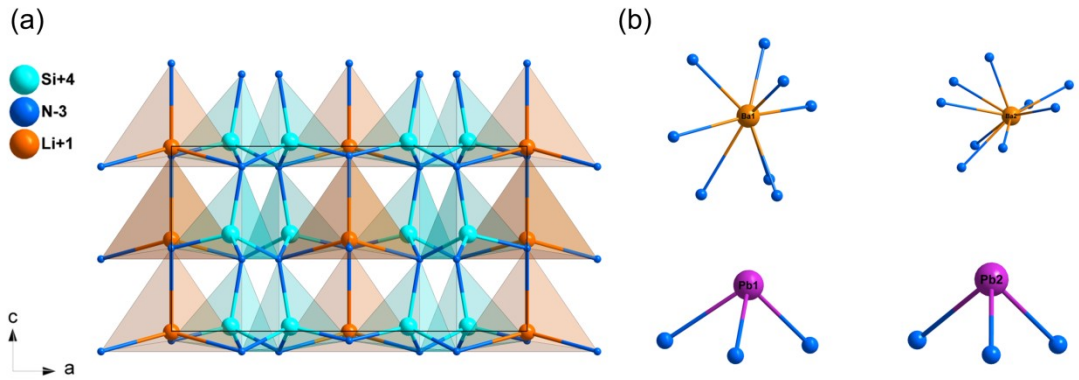

Figure S1 Crystal structure of $LiSi_2N_3$ (a); coordination of Ba^{2+} / Pb^{2+} in $Ba_2Si_5N_8$ / $Pb_2Si_5N_8$ (b).

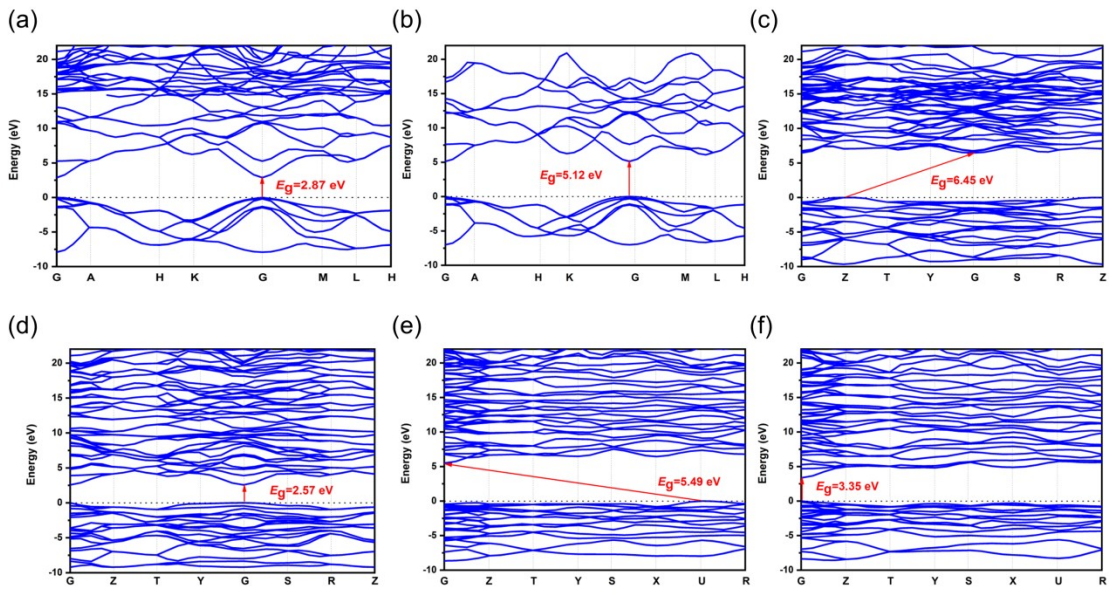

Figure S2 Calculated band structure (HSE06) of GaN (a), AlN (b), $LiSi_2N_3$ (c), $LiGe_2N_3$ (d), $MgSiN_2$ (e) and $MgGeN_2$ (f).

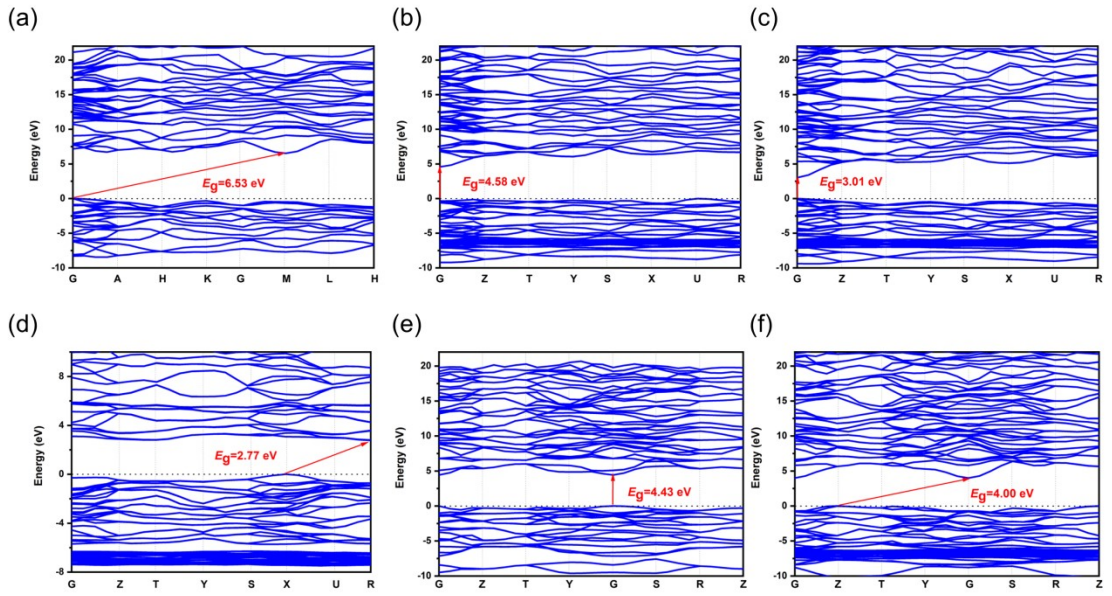

Figure S3 Calculated band structure (HSE06) of $BeSiN_2$ (a), $ZnSiN_2$ (b), $ZnGeN_2$ (c), Zn_3MoN_4 (d), Mg_2PN_3 (e) and Zn_2PN_3 (f).

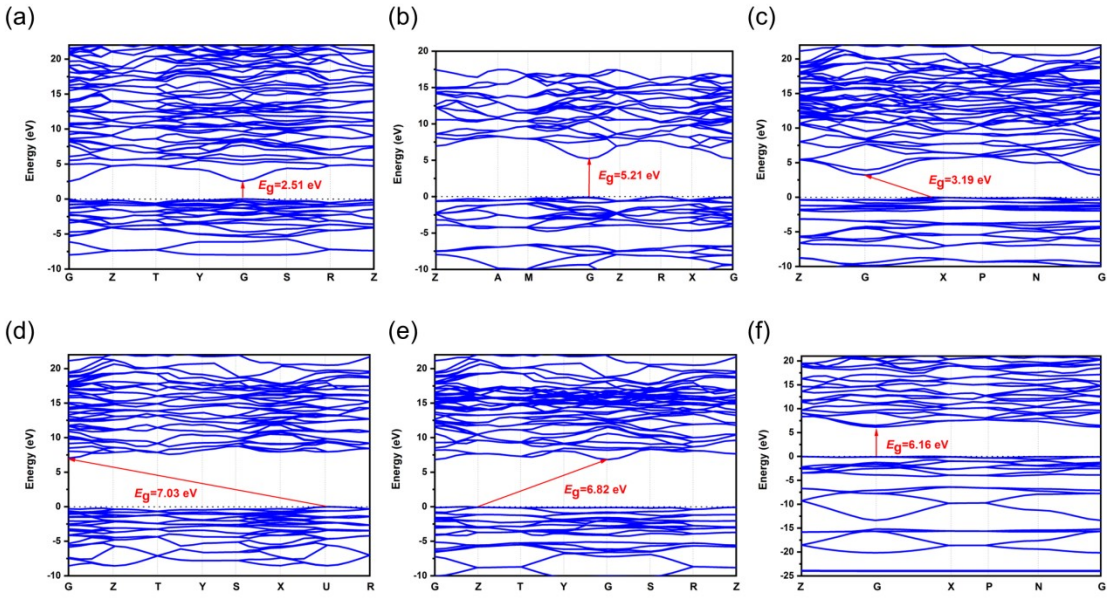

Figure S4 Calculated band structure (HSE06) of $MgSbN_3$ (a), $LiPN_2$ (b), $CuPN_2$ (c), LiSiON (d), Li_2PO_2N (e) and $NaPN_2$ (f).

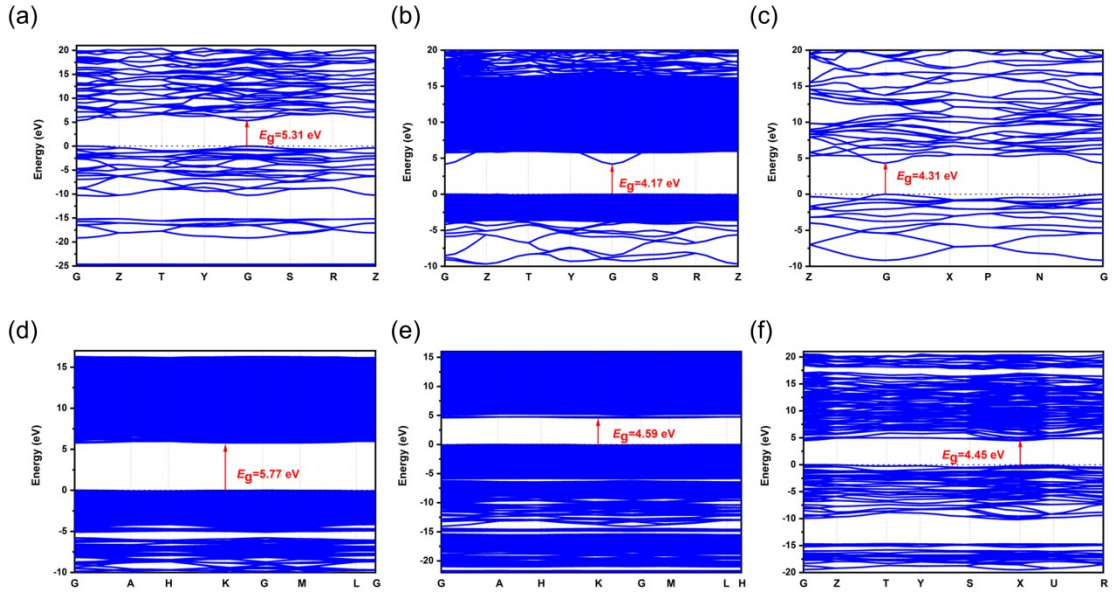

Figure S5 Calculated band structure (HSE06) of $NaSi_2N_3$ (a), $NaGe_2N_3$ (b), $CaGeN_2$ (c), CaP_2N_4 (d), SrP_2N_4 (e) and $Sr_2Si_5N_8$ (f).

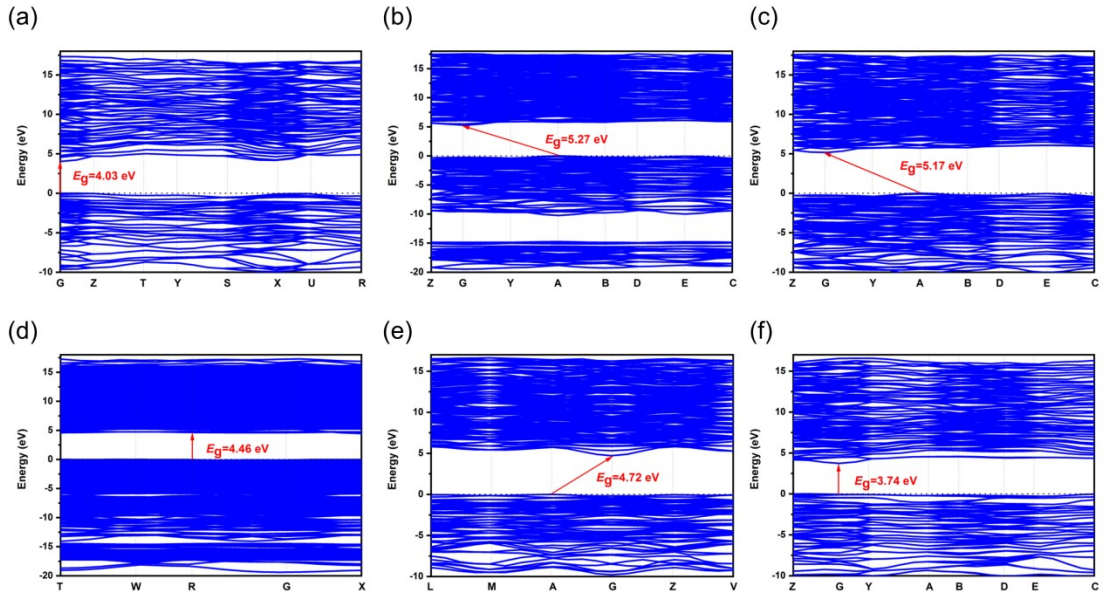

Figure S6 Calculated band structure (HSE06) of $Ba_2Si_5N_8$ (a), $SrSi_7N_{10}$ (b), $BaSi_7N_{10}$ (c), $SrSi_6N_8$ (d), α-$Ca_2Si_5N_8$ (e) and β-$Ca_2Si_5N_8$ (f).

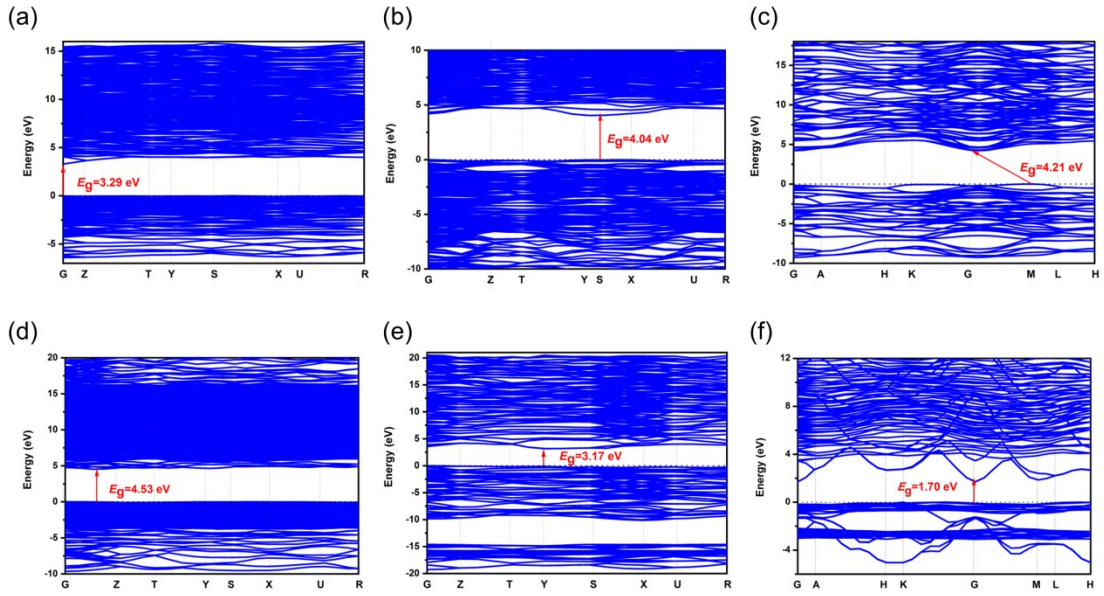

Figure S7. Calculated band structure (HSE06) of $Ca_3Al_2N_4$ (a), $SrAlSi_4N_7$ (b), $SrYSi_4N_7$ (c), $LaSi_3N_5$ (d), $Pb_2Si_5N_8$ (e) and NaSnN (f).

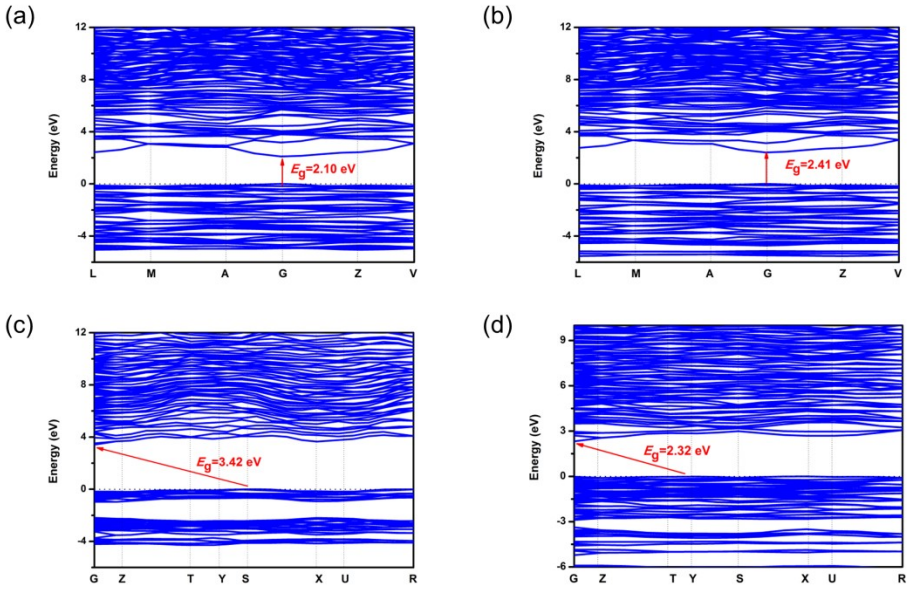

Figure S8 Calculated band structure (HSE06) of Na_3MoN_4 (a), Na_3WN_4 (b), $Ba_3B_2N_4$ (c), $Ba_5Si_2N_6$ (d).

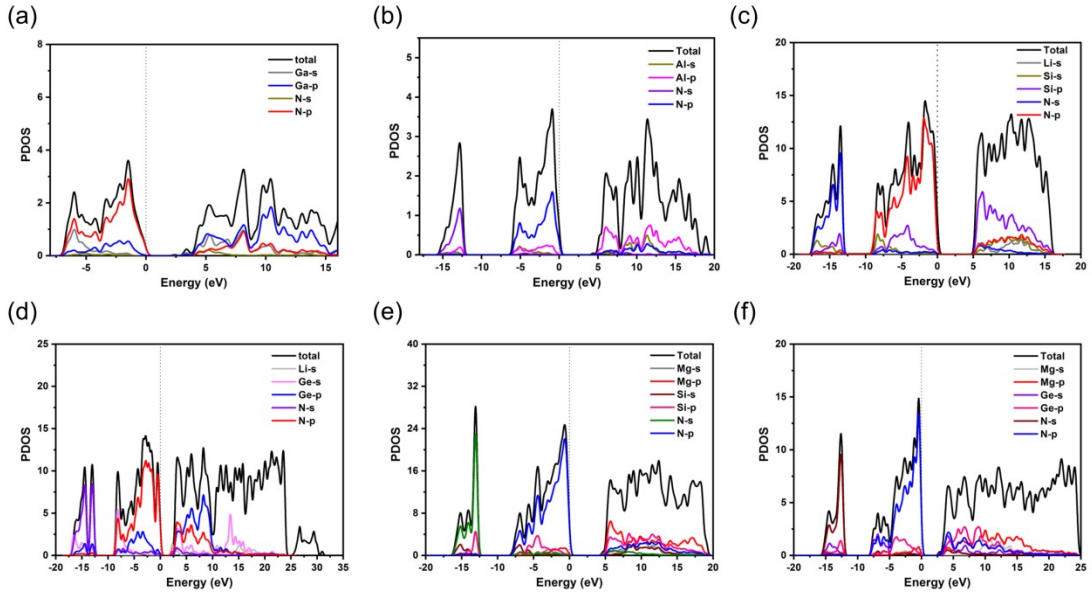

Figure S9 Total density/partial density of states (PDOS) of GaN (a), AlN (b), $LiSi_2N_3$ (c), $LiGe_2N_3$ (d), $MgSiN_2$ (e), and $MgGeN_2$ (f).

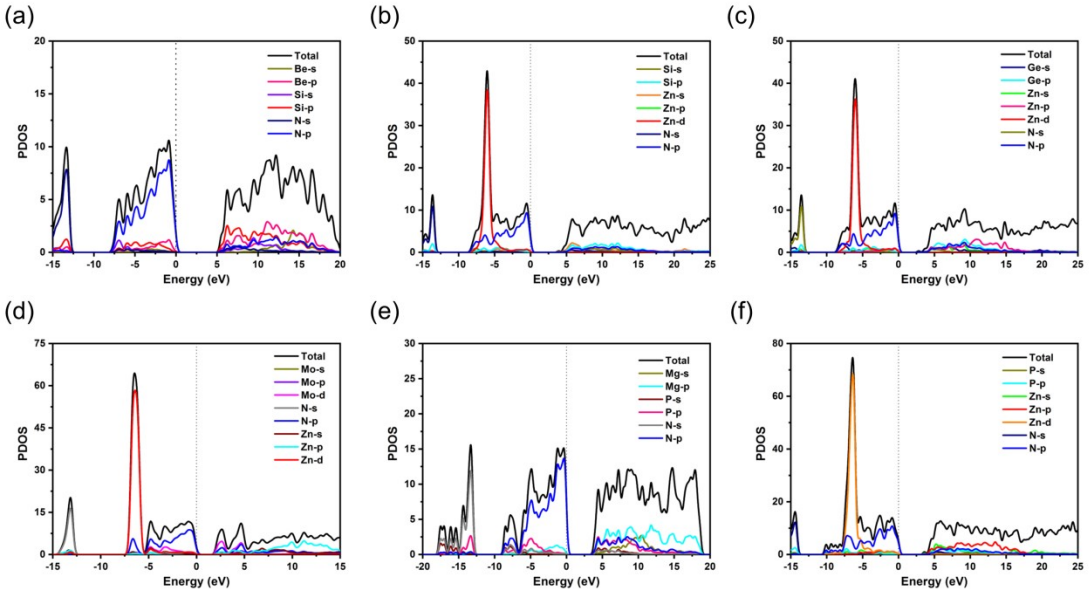

Figure S10 Total density/partial density of states (PDOS) of $BeSiN_2$ (a), $ZnSiN_2$ (b), $ZnGeN_2$ (c), Zn_3MoN_4 (d), Mg_2PN_3 (e), and Zn_2PN_3 (f).

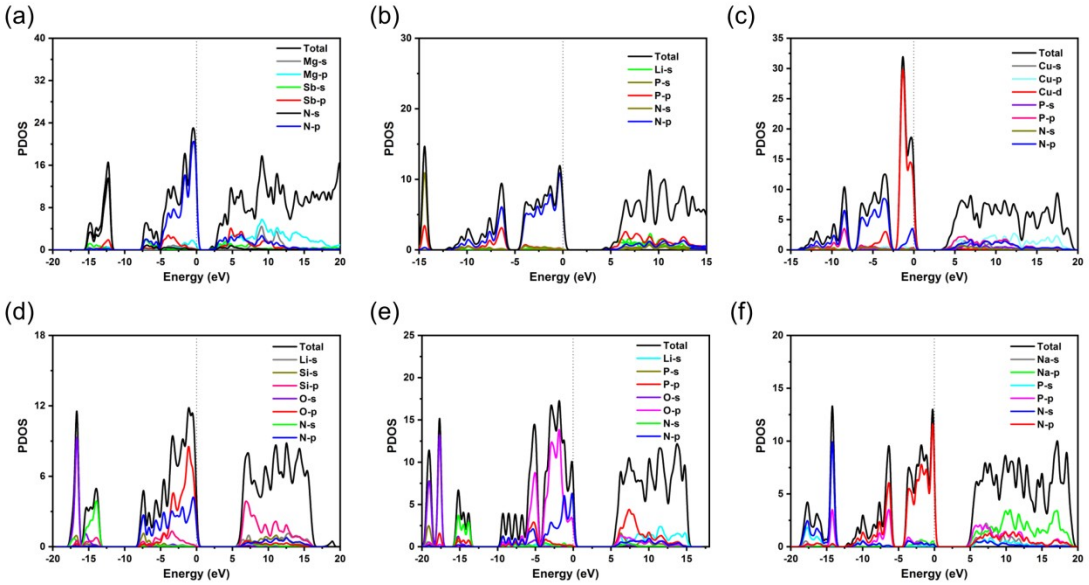

Figure S11 Total density/partial density of states (PDOS) of $MgSbN_3$ (a), $LiPN_2$ (b), $CuPN_2$ (c), LiSiON (d), Li_2PO_2N (e), and $NaPN_2$ (f).

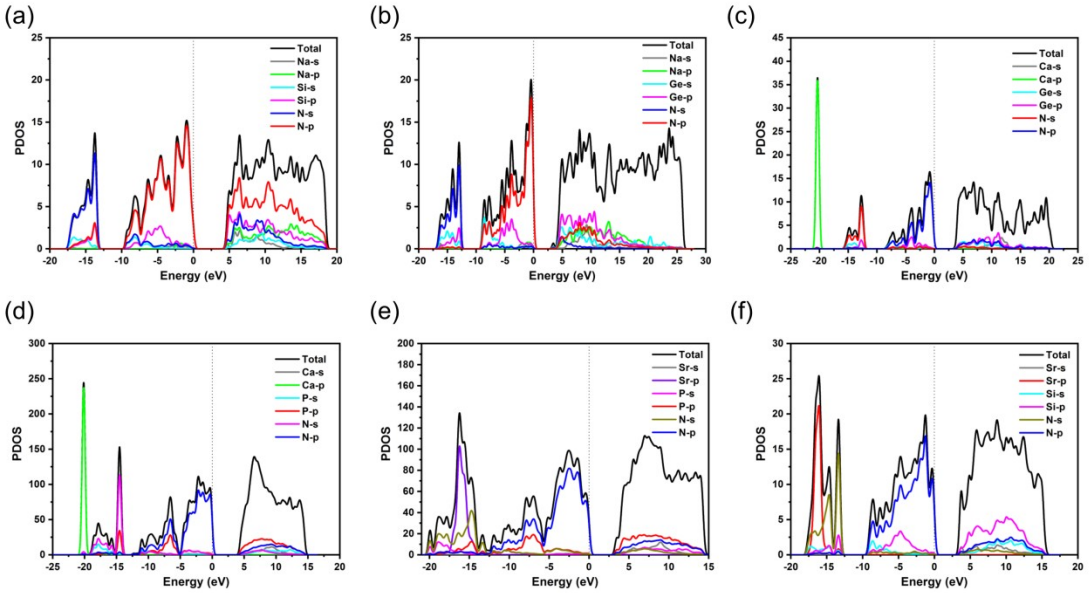

Figure S12 Total density/partial density of states (PDOS) of NaSi2N3 (a), NaGe2N3 (b), CaGeN2 (c), CaP2N4 (d), SrP2N4 (e), and Sr2Si5N8 (f).

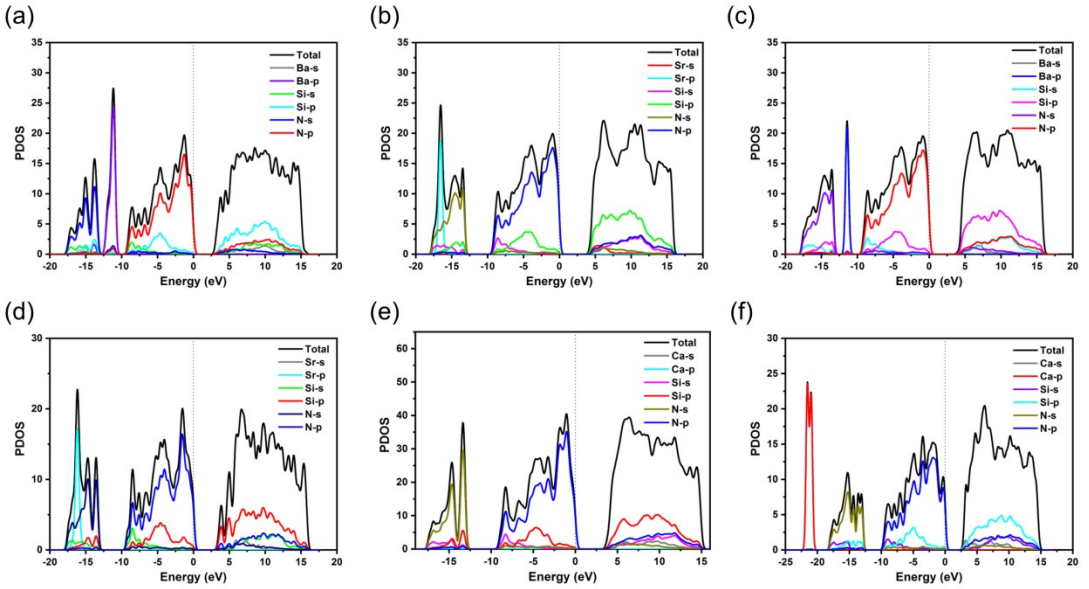

Figure S13 Total density/partial density of states (PDOS) of $Ba_2Si_5N_8$ (a), $SrSi_7N_{10}$ (b), $BaSi_7N_{10}$ (c), $SrSi_6N_8$ (d), α-$Ca_2Si_5N_8$ (e), and β-$Ca_2Si_5N_8$ (f).

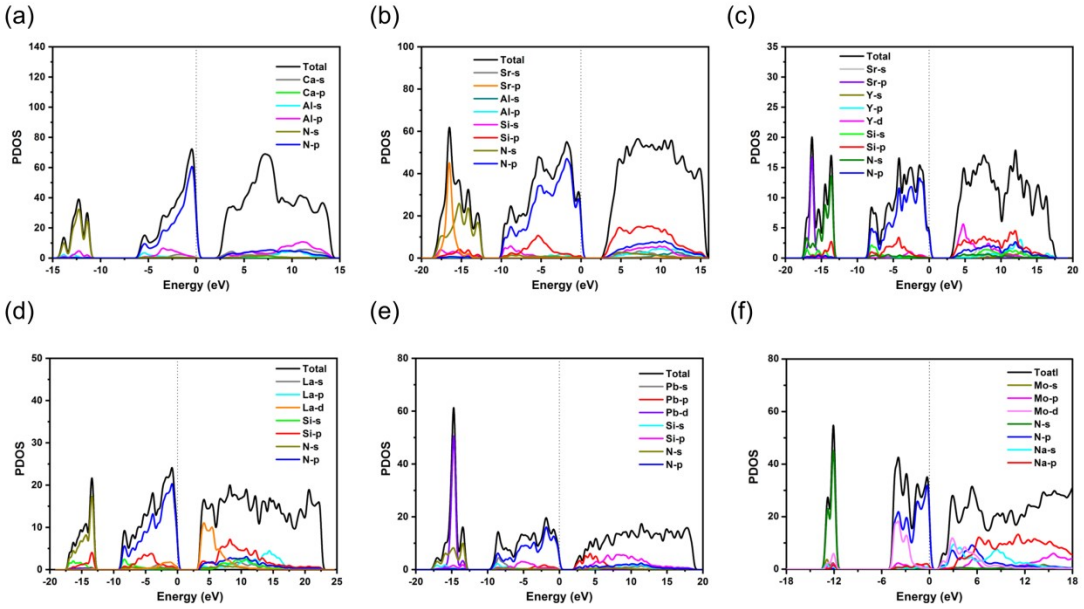

Figure S14 Total density/partial density of states (PDOS) of $Ca_3Al_2N_4$ (a), $SrAlSi_4N_7$ (b), $SrYSi_4N_7$ (c), $LaSi_3N_5$ (d), $Pb_2Si_5N_8$ (e), and Na_3MoN_4 (f).

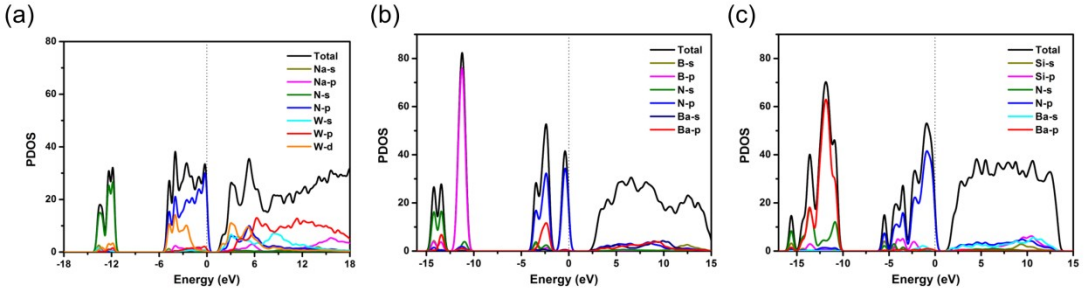

Figure S15 Total density/partial density of states (PDOS) of Na_3WN_4 (a), $Ba_3B_2N_4$ (c), and $Ba_5Si_2N_6$ (c).

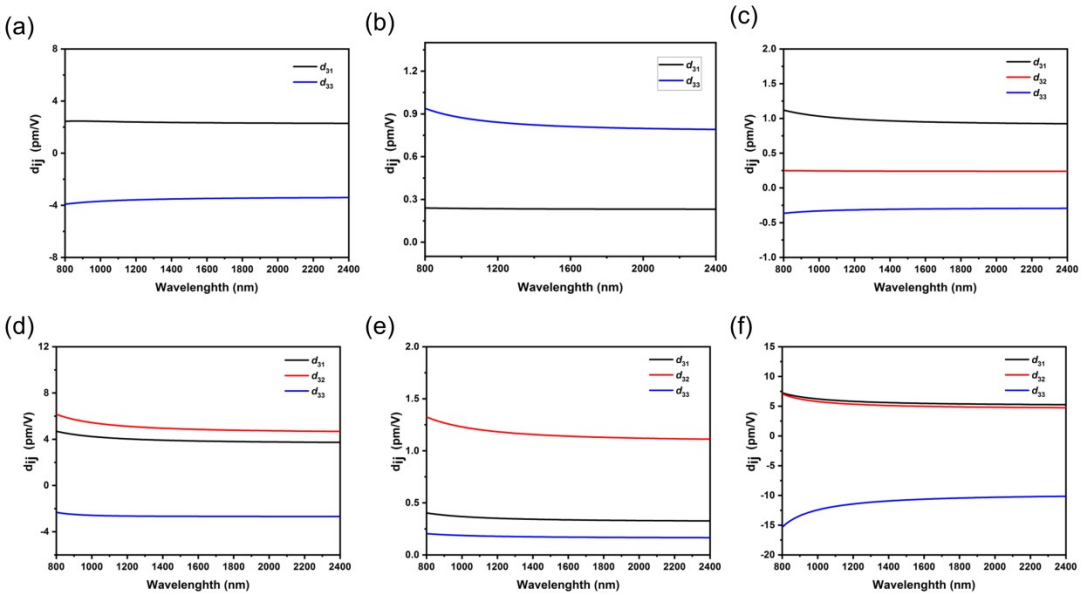

Figure S16 Calculated frequency-dependent coefficients of GaN (a), AlN (b), $LiSi_2N_3$ (c), $LiGe_2N_3$ (d), $MgSiN_2$ (e), and $MgGeN_2$ (f).

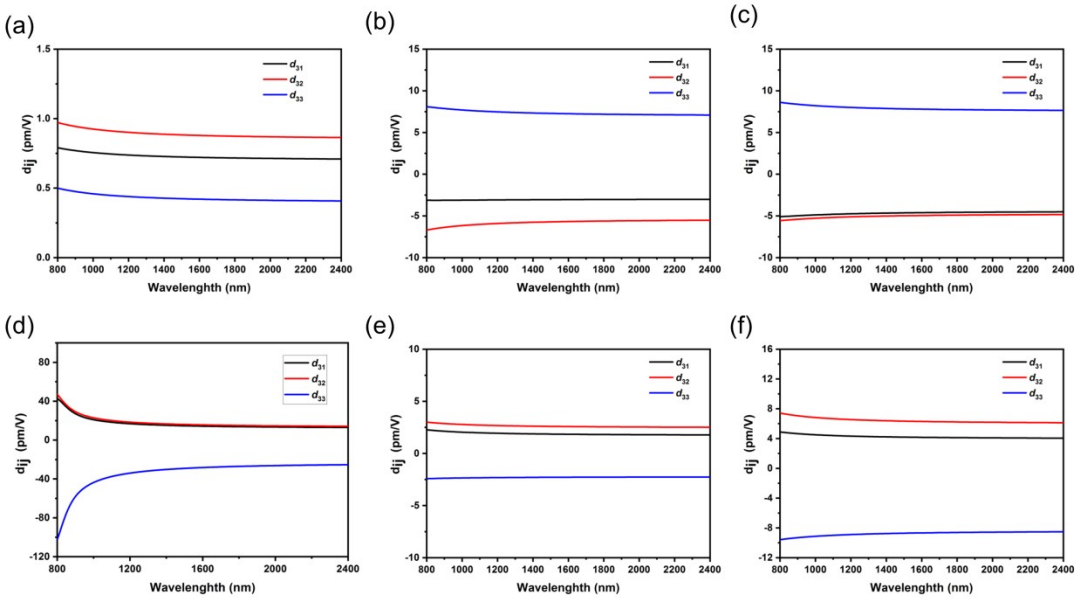

Figure S17 Calculated frequency-dependent coefficients of $BeSiN_2$ (a), $ZnSiN_2$ (b), $ZnGeN_2$ (c), Zn_3MoN_4 (d), Mg_2PN_3 (e), and Zn_2PN_3 (f).

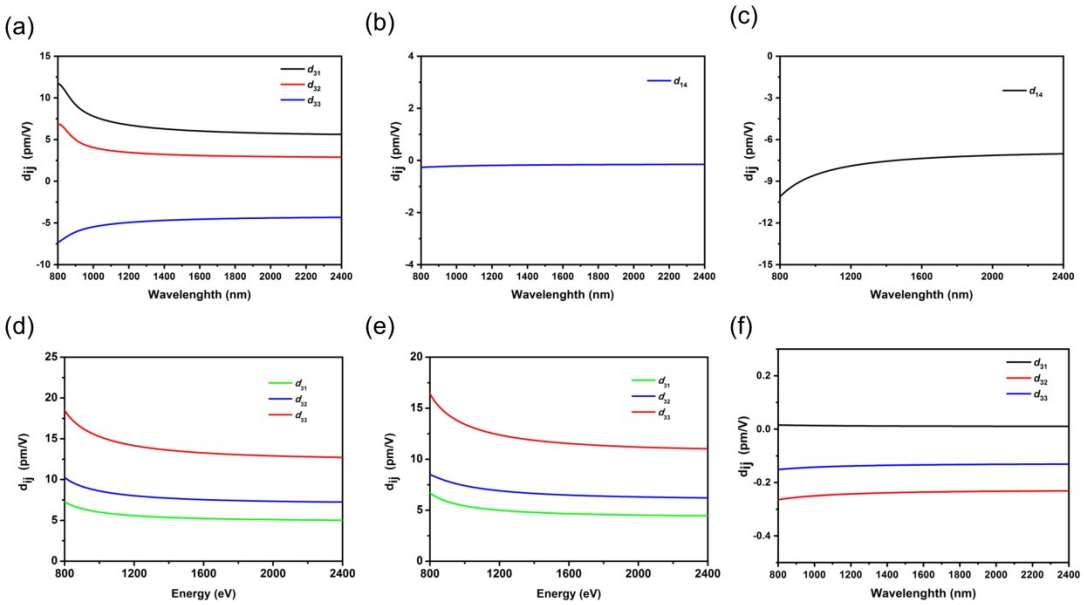

Figure S18 Calculated frequency-dependent coefficients of $MgSbN_3$ (a), $LiPN_2$ (b), $CuPN_2$ (c), Zn_2NCl (d), Zn_2NBr (e), and LiSiON (f).

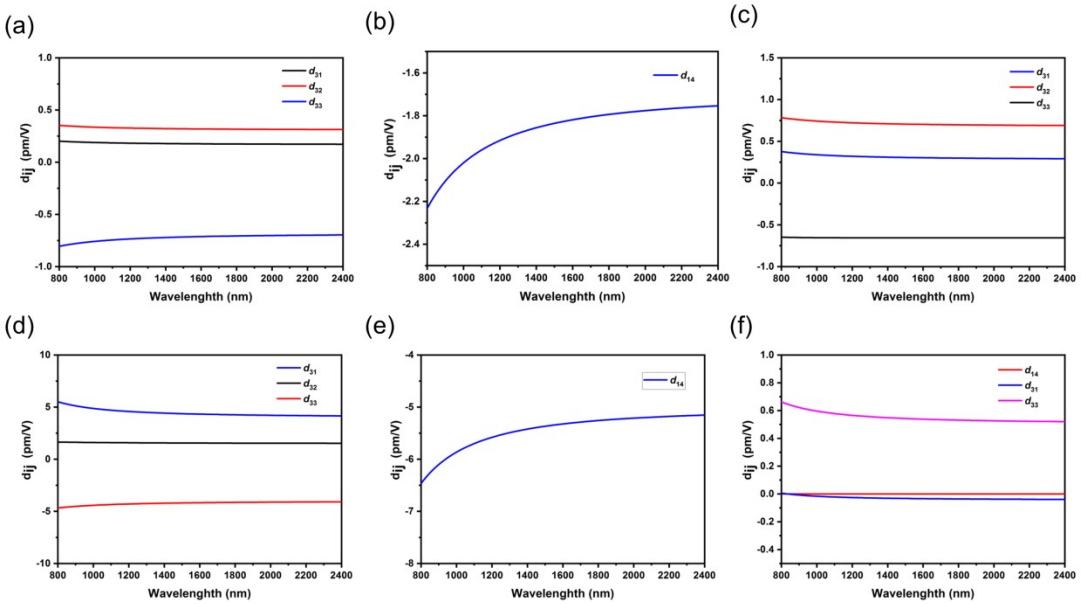

Figure S19 Calculated frequency-dependent coefficients of $LiPO_2N$ (a), $NaPN_2$ (b), $NaSi_2N_3$ (c), $NaGe_2N_3$ (d), $CaGeN_2$ (e), and CaP_2N_4 (f).

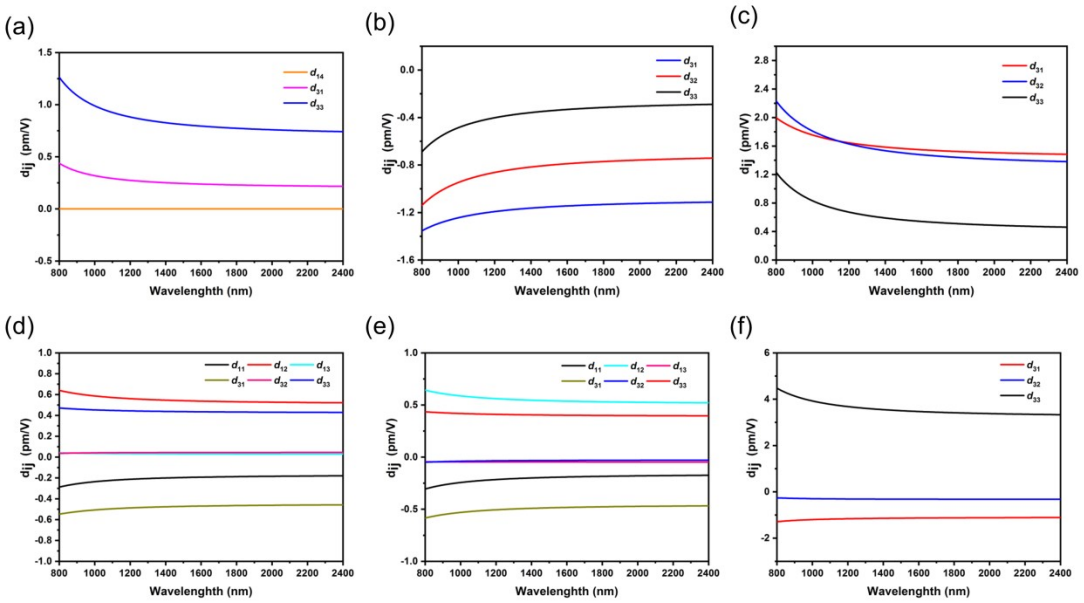

Figure S20 Calculated frequency-dependent coefficients of SrP_2N_4 (a), $Sr_2Si_5N_8$ (b), $Ba_2Si_5N_8$ (c), $SrSi_7N_{10}$ (d), $BaSi_7N_{10}$ (e), and $SrSi_6N_8$ (f).

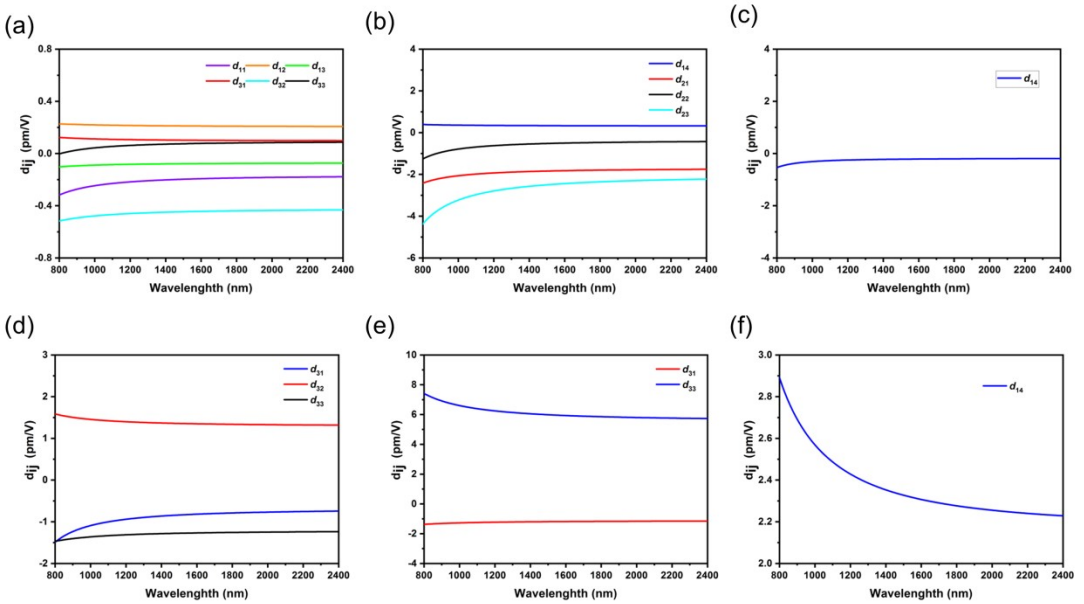

Figure S21 Calculated frequency-dependent coefficients of α-$Ca_2Si_5N_8$ (a), β-$Ca_2Si_5N_8$ (b), $Ca_3Al_2N_4$ (c), $SrAlSi_4N_7$ (d), $SrYSi_4N_7$ (e), and $LaSi_3N_5$ (f).

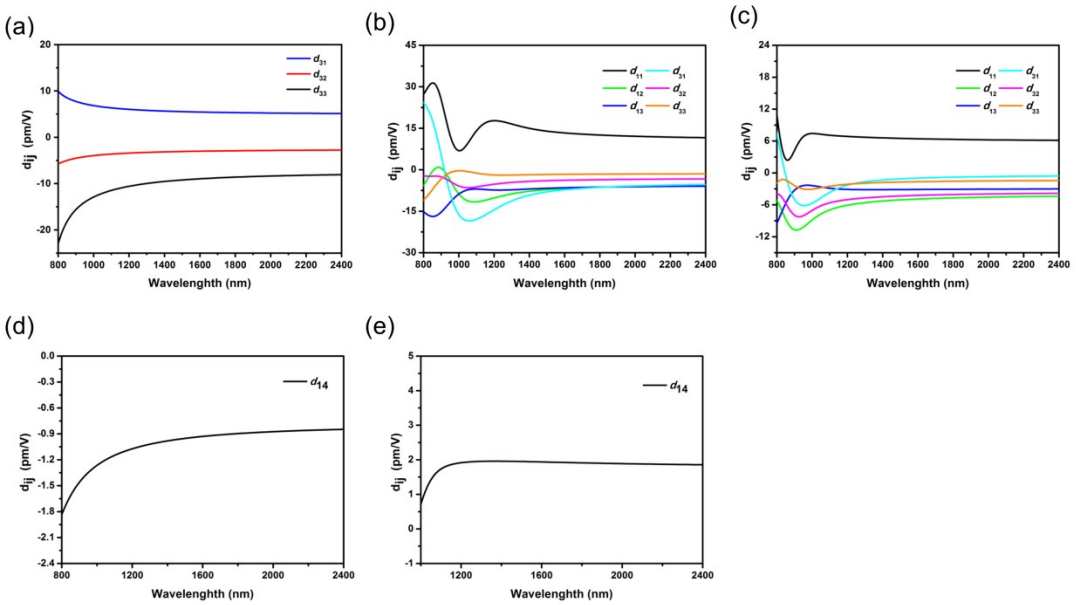

Figure S22 Calculated frequency-dependent coefficients of $Pb_2Si_5N_8$ (a), Na_3MoN_4 (b), Na_3WN_4 (c), $Ba_3B_2N_4$ (d), and $Ba_5Si_2N_6$ (e).

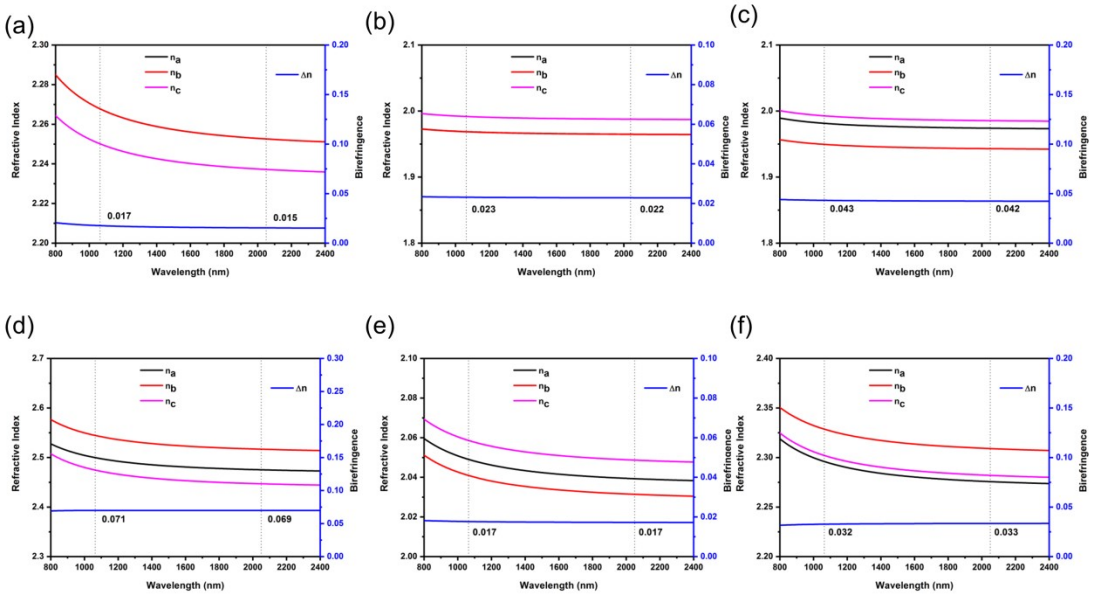

Figure S23 The calculated refractive index dispersion curves and birefringence of GaN (a), AlN (b), $LiSi_2N_3$ (c), $LiGe_2N_3$ (d), $MgSiN_2$ (e), and $MgGeN_2$ (f).

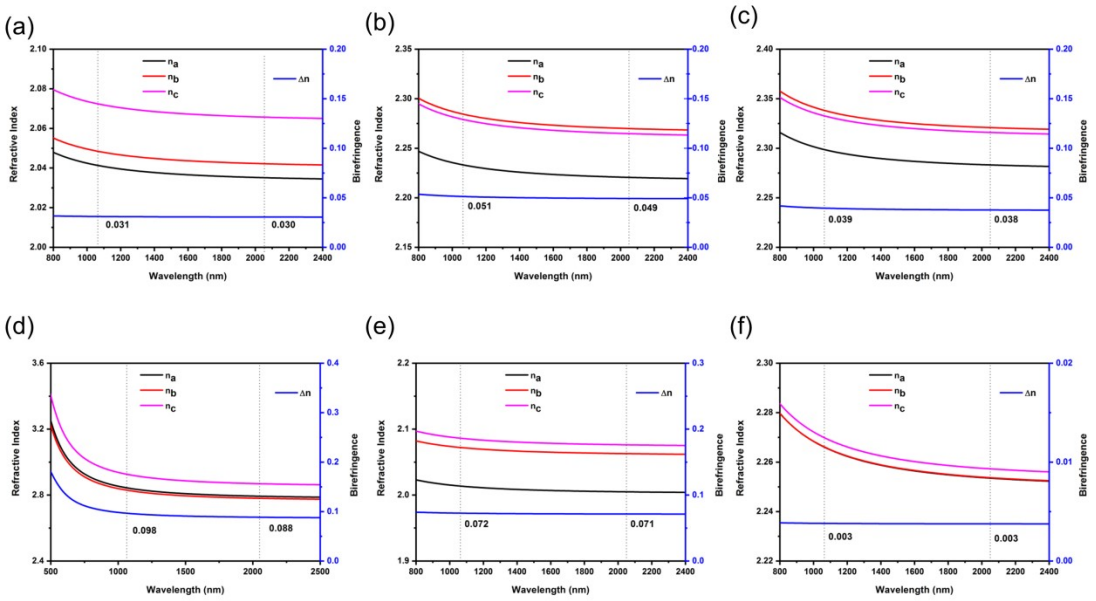

Figure S24 The calculated refractive index dispersion curves and birefringence of $BeSiN_2$ (a), $ZnSiN_2$ (b), $ZnGeN_2$ (c), Zn_3MoN_4 (d), Mg_2PN_3 (e), and Zn_2PN_3 (f).

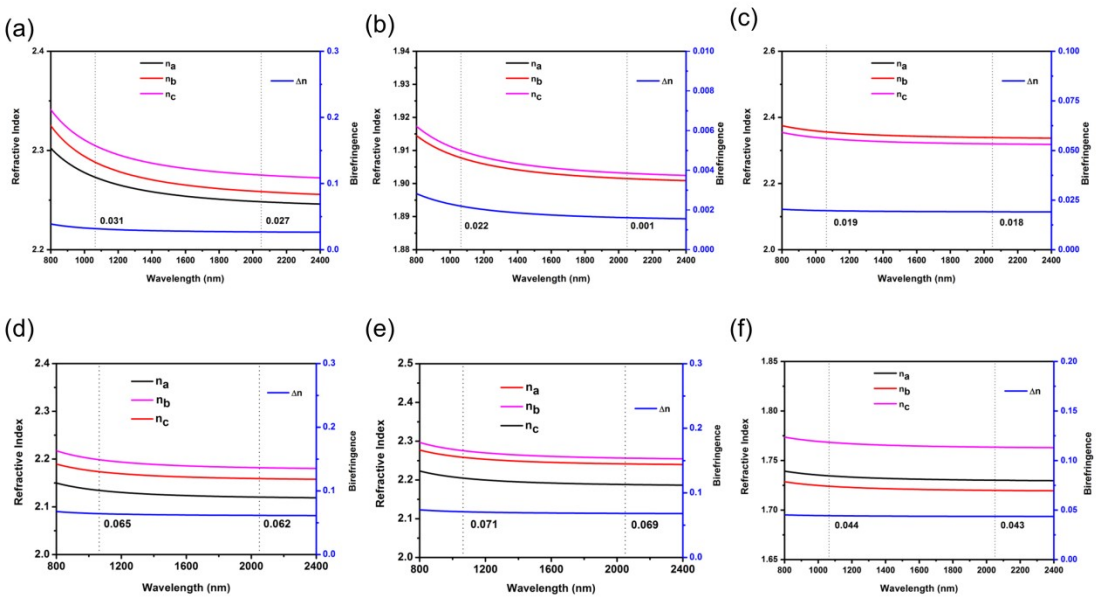

Figure S25 The calculated refractive index dispersion curves and birefringence of $MgSbN_3$ (a), $LiPN_2$ (b), $CuPN_2$ (c), Zn_2NCl (d), Zn_2NBr (e), and LiSiON (f).

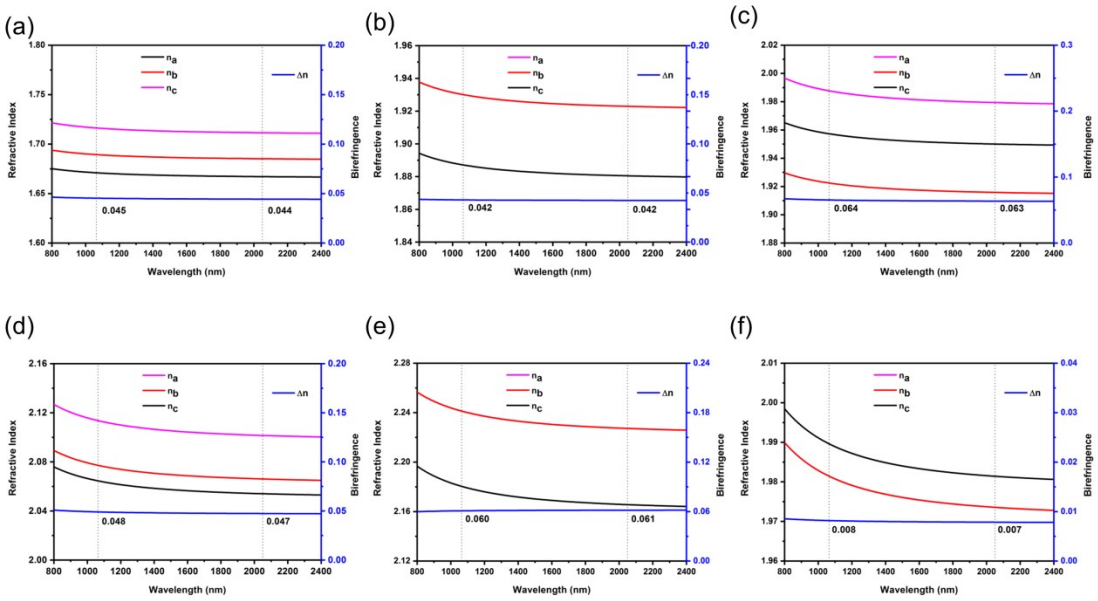

Figure S26 The calculated refractive index dispersion curves and birefringence of $LiPO_2N$ (a), $NaPN_2$ (b), $NaSi_2N_3$ (c), $NaGe_2N_3$ (d), $CaGeN_2$ (e), and CaP_2N_4 (f).

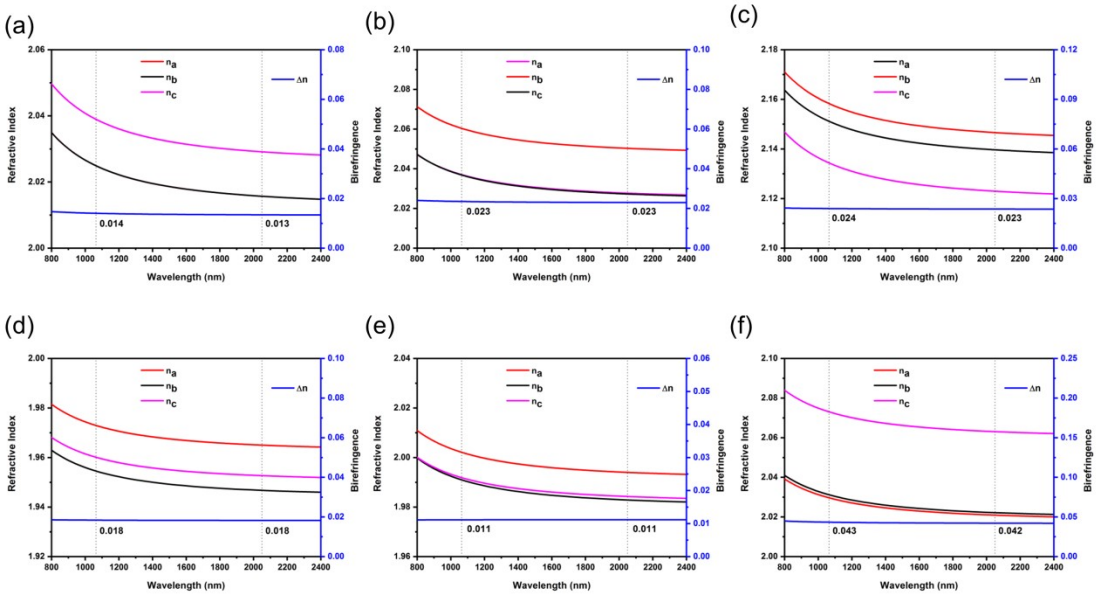

Figure S27 The calculated refractive index dispersion curves and birefringence of SrP_2N_4 (a), $Sr_2Si_5N_8$ (b), $Ba_2Si_5N_8$ (c), $SrSi_7N_{10}$ (d), $BaSi_7N_{10}$ (e), and $SrSi_6N_8$ (f).

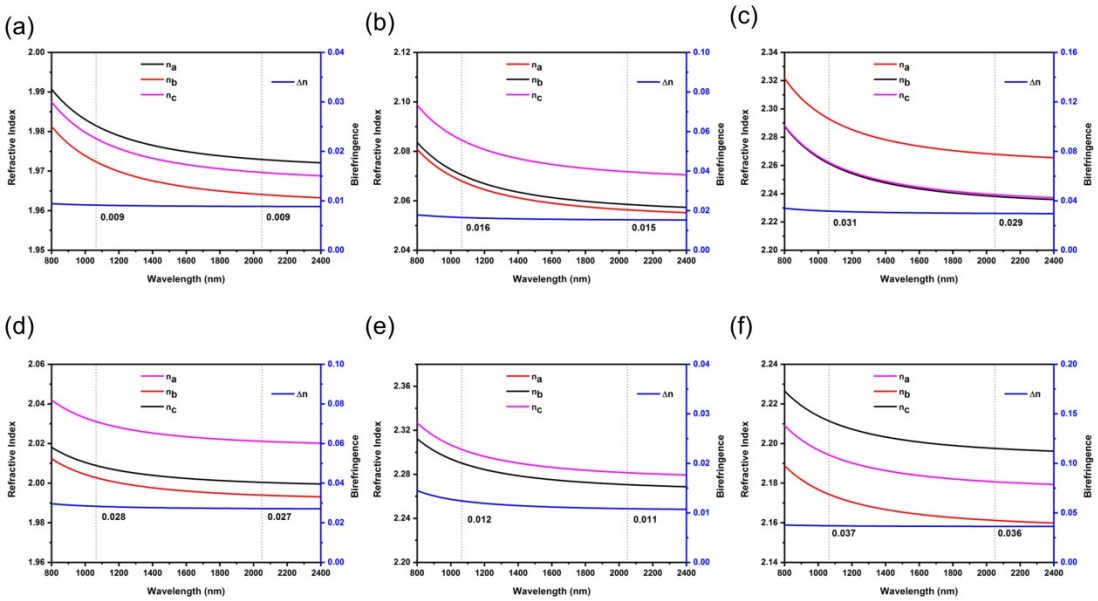

Figure S28 The calculated refractive index dispersion curves and birefringence of α-Ca2Si5N8 (a), β-Ca2Si5N8 (b), Ca3Al2N4 (c), SrAlSi4N7 (d), SrYSi4N7 (e), and LaSi3N5 (f).

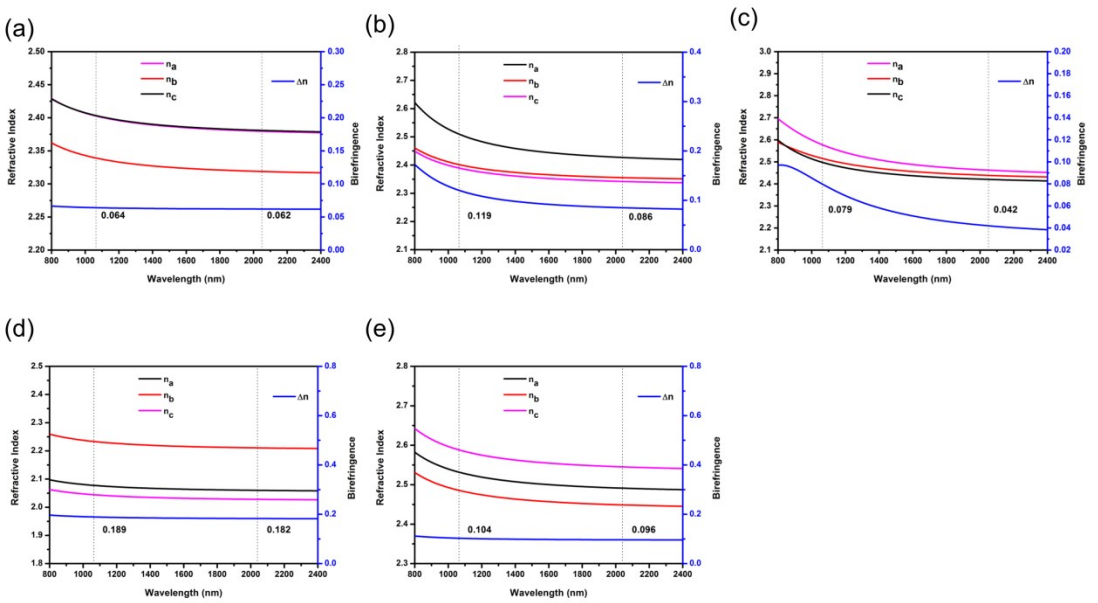

Figure S29 The calculated refractive index dispersion curves and birefringence of $Pb_2Si_5N_8$ (a), Na_3MoN_4 (b), Na_3WN_4 (c), $Ba_3B_2N_4$ (d), and $Ba_5Si_2N_6$ (e).

References

1 S. J. Clark, M. D. Segall, C. J. Pickard, P. J. Hasnip, M. J. Probert, K. Refson and M. C. Payne, First principles methods using CASTEP, *Z. Kristall.,* 2005, **220**, 567-570.

2 J. P. Perdew, K. Burke and M. Ernzerhof, Generalized gradient approximation made simple, *Phys. Rev. Lett.*, 1996, **77**, 3865-3868.

3 A. M. Rappe, K. M. Rabe, E. Kaxiras and J. D. Joannopoulos, Optimized pseudopotentials, *Phys. Rev. B*, 1990, **41**, 1227-1230.

4 J. S. Lin, A. Qteish, M. C. Payne and V. Heine, Optimized and transferable nonloca separable abinitio pseudopotentials, *Phys. Rev. B*, 1993, **47**, 4174-4180.

5 L. Kang, M. L. Zhou, J. Y. Yao, Z. S. Lin, Y. C. Wu and C. T. Chen, Metal Thiophosphates with Good Mid-infrared Nonlinear Optical Performances: A First-Principles Prediction and Analysis, *J. Am. Chem. Soc.*, 2015, **137**, 13049-13059.

6 J. Yu, B. B. Zhang, X. D. Zhang, Y. Wang, K. Wu and M. H. Lee, Finding Optimal Mid-Infrared Nonlinear Optical Materials in Germanates by First-Principles High-Throughput Screening and Experimental Verification, *ACS Appl. Mater. Interfaces*, 2020, **12**, 45023-45035.

7 X. D. Zhang, L. C. Guo, B. B. Zhang, J. Yu, Y. Wang, K. Wu, H. J. Wang and M. H. Lee, From silicates to oxonitridosilicates: improving optical anisotropy for phase-matching as ultraviolet nonlinear optical materials, *Chem. Commun.*, 2021, **57**, 639-642.

8 W. D. Cheng, C. S. Lin, H. Zhang and G. L. Chai, Theoretical Evaluation on Terahertz Source Generators from Ternary Metal Chalcogenides of PbM_6Te_{10} (M = Ga, In), *J. Phys. Chem. C*, 2018, **122**, 4557-4564.

9 D. J. Moss, E. Ghahramani, J. E. Sipe and H. M. Vandriel, Band-structure calculation of dispersion and anisotropy in $\chi^{(3)}$ for third-harmonic generation in Si, Ge, and GaAs, *Phys. Rev. B*, 1990, **41**, 1542-1560.